Table 2 **Preliminary data on carbon solubility in mantle minerals**

Run no.	*T* (°C)	*P* (GPa)	Duration (h)	Carbon (wt p.p.m.)
E9 (enstatite)	900	1.5	96	4.7 3.0 Not detected
Di9 (diopside)	900	1.5	168	0.5 0.4
Py6/5 (pyrope)	1,300	6	10	2.1 1.9
Sp24 (spinel)	1,100	1.5	168	Not detected

Each carbon concentration refers to a single analysis on an individual crystal. Concentrations in wt p.p.m. are recalculated for carbon of normal isotopic composition. For errors see text. Sample E9 appears to be inhomogeneous and may contain submicroscopic inclusions so that the data should be considered as an upper limit of carbon solubility only. Experiment Py6/5 was carried out in a multi-anvil apparatus, all other experiments were conducted in a piston cylinder press.

melt is independent of oxygen fugacity, since the oxidation state of carbon in both coexisting phases is the same.

Bulk mantle carbon abundances have been estimated to be of the order of several hundred to more than 1,000 p.p.m. by weight[2]. For the depleted MORB source, some very low values of 72–270 p.p.m. by weight of CO_2 have recently been derived from the analyses of undegassed melt inclusions[18–19]. Abundances in undepleted mantle sources should be much higher. By comparing any of these numbers with the measured carbon solubilities it is evident that this carbon cannot be present in olivine or any other major mineral of the upper mantle. Instead, it must reside in a separate carbon-rich phase. Extensive experimental research in the 1970s has demonstrated that only CO_2-rich fluids and carbonates are plausible phases for storing carbon in the mantle[6,7], if it is not dissolved in silicate minerals. CO_2 reacts with olivine at pressures above 2–3 GPa to form carbonates according to reactions of the type $MgCO_3 + MgSiO_3 = Mg_2SiO_4 + CO_2$. Therefore, carbonates appear to host more than 90% of the carbon present in the deeper part of the upper mantle. This situation is very different from that observed for hydrogen, another volatile element, where it has been demonstrated that the entire mantle reservoir can be incorporated in nominally anhydrous minerals such as olivine[20,21].

Our results have profound implications for the dynamics of the global carbon cycle. If traces of carbon were stored as a solid solution in olivine, releasing large quantities of carbon to the atmosphere would be virtually impossible on short timescales because of the slow diffusion coefficients of carbon in olivine, and because during normal melting events, only a little olivine is dissolved in the magma. For the same reasons, the exchange of hydrogen between the Earth's mantle and the hydrosphere is slow and the volume of the oceans has changed little over the last three billion years. However, carbonates are easily mobilized during even low degrees of partial melting, and upon decompression below 2.5 to 3.5 GPa they decompose and release CO_2 (refs 6, 7). Moreover, geochemical evidence suggests a highly inhomogeneous distribution of carbon throughout the mantle[2,16,18]. It is therefore conceivable that a large melting event in a carbonate-rich part of the deeper mantle could rapidly transfer large amounts of carbon dioxide into the atmosphere. This is consistent with models that link extinction events, such as the event at the Triassic–Jurassic boundary, to flood basalt eruptions via a sudden increase of global CO_2 levels[8–10]. □

Received 1 April; accepted 13 June 2003; doi:10.1038/nature01828.

1. Javoy, M., Pineau, F. & Allègre, C. J. Carbon geodynamic cycle. *Nature* **300,** 171–173 (1982).
2. Jambon, A. Earth degassing and large-scale geochemical cycling of volatile elements. *Rev. Mineral.* **30,** 479–517 (1994).
3. Zhang, Y. & Zindler, A. Distribution and evolution of carbon and nitrogen in Earth. *Earth Planet. Sci. Lett.* **117,** 331–345 (1993).
4. Green, H. W. A CO_2-charged asthenosphere. *Nature* **238,** 2–5 (1972).
5. Green, H. W. & Radcliffe, S. V. Fluid precipitates in rocks from the Earth's mantle. *Geol. Soc. Am. Bull.* **86,** 846–852 (1975).
6. Newton, R. C. & Sharp, W. E. Stability of forsterite $+CO_2$ and its bearing on the role of CO_2 in the mantle. *Earth Planet. Sci. Lett.* **26,** 239–244 (1975).
7. Wyllie, P. J. & Huang, W. L. Carbonation and melting reactions in the system CaO-MgO-SiO_2-CO_2 at mantle pressures with geophysical and petrological applications. *Contrib. Mineral. Petrol.* **54,** 79–107 (1976).
8. McElwain, J. C., Beerling, D. J. & Woodward, F. I. Fossil plants and global warming at the Triassic-Jurassic boundary. *Science* **285,** 1386–1390 (1999).
9. Beerling, D. CO_2 and the end-Triassic mass extinction. *Nature* **415,** 386–387 (2002).
10. Marzoli, A. *et al.* Extensive 200-million-year-old continental flood basalts of the central Atlantic magmatic province. *Science* **284,** 616–618 (1999).
11. Kerrick, D. M. Present and past nonanthropogenic CO_2 degassing from the solid Earth. *Rev. Geophys.* **39,** 565–585 (2001).
12. Freund, F., Kathrein, H., Wengeler, H., Knobel, R. & Heinen, H. J. Carbon in solid solution in forsterite — A key to the untraceable nature of reduced carbon in terrestrial and cosmogenic rocks. *Geochim. Cosmochim. Acta* **44,** 1319–1333 (1980).
13. Mathez, E. A., Blacic, J. D., Berry, J., Hollander, M. & Maggiore, C. Carbon in olivine: Results from nuclear reaction analysis. *J. Geophys. Res.* **92,** 3500–3506 (1987).
14. Tingle, T. N., Green, H. W. & Finnerty, A. A. Experiments and observations bearing on the solubility and diffusivity of carbon in olivine. *J. Geophys. Res.* **93,** 15289–15304 (1988).
15. Tsong, I. S. T., Knipping, U., Loxton, C. M., Magee, C. W. & Arnold, G. W. Carbon on surfaces of magnesium oxide and olivine single crystals. Diffusion from the bulk or surface contamination? *Phys. Chem. Minerals* **12,** 261–270 (1985).
16. Hauri, E. H., Shimizu, N., Dieu, J. J. & Hart, S. R. Evidence for hotspot-related carbonatite metasomatism in the oceanic upper mantle. *Nature* **365,** 221–227 (1993).
17. Putnis, A. *Introduction to Mineral Sciences* (Cambridge Univ. Press, Cambridge, 1992).
18. Hauri, E., Gronvold, K., Oskarsson, N., McKenzie, D. Abundance of carbon in the Icelandic mantle: Constraints from melt inclusions. *Eos* **83**, 383 (2002).
19. Saal, A. E., Hauri, E. H., Langmuir, C. H. & Perfit, M. R. Vapour undersaturation in primitive mid-ocean-ridge basalt and the volatile content of Earth's upper mantle. *Nature* **419,** 451–455 (2002).
20. Bell, D. R. & Rossman, G. R. Water in the Earth's mantle: The role of nominally anhydrous minerals. *Science* **255,** 1391–1397 (1992).
21. Kohlstedt, D. L., Keppler, H. & Rubie, D. C. Solubility of water in the α, β and γ phases of $(Mg,Fe)_2SiO_4$. *Contrib. Mineral. Petrol.* **123,** 345–357 (1995).

Supplementary Information accompanies the paper on **www.nature.com/nature**.

Acknowledgements We thank D. Frost for technical assistance with one multi-anvil experiment at Bayerisches Geoinstitut, Bayreuth; we also thank R. Brooker for comments and suggestions. This study was supported by the German Science Foundation (DFG, Leibniz award to H.K.).

Competing interests statement The authors declare that they have no competing financial interests.

Correspondence and requests for materials should be addressed to H.K. (Hans.Keppler@uni-tuebingen.de).

Reflection signature of seismic and aseismic slip on the northern Cascadia subduction interface

Mladen R. Nedimović*, Roy D. Hyndman†, Kumar Ramachandran† & George D. Spence‡

** Lamont-Doherty Earth Observatory of Columbia University, 61 Route 9W, PO Box 1000, Palisades, New York, 10964-8000, USA*
† Pacific Geoscience Centre, Geological Survey of Canada, Sidney, British Columbia, V8L 4B2, Canada and ‡ School of Earth and Ocean Sciences, University of Victoria, Victoria, British Columbia, V8W 3P6, Canada

At the northern Cascadia margin, the Juan de Fuca plate is underthrusting North America at about 45 mm yr^{-1} (ref. 1), resulting in the potential for destructive great earthquakes[2,3]. The downdip extent of coupling between the two plates is difficult to determine because the most recent such earthquake (thought to have been in 1700)[4] occurred before instrumental recording. Thermal and deformation studies[5] indicate that, off southern Vancouver Island, the interplate interface is presently fully locked for a distance of ~60 km downdip from the deformation front. Great thrust earthquakes on this section of the interface (with magnitudes of up to 9)[4,5] have been estimated to occur at an average interval of about 590 yr (ref. 3). Further downdip there is a transition from fully locked behaviour to aseismic sliding (where high temperatures allow ductile

deformation), with the deep aseismic zone exhibiting slow-slip thrust events[6]. Here we show that there is a change in the reflection character on seismic images from a thin sharp reflection where the subduction thrust is inferred to be locked, to a broad reflection band at greater depth where aseismic slip is thought to be occurring. This change in reflection character may provide a new technique to map the landward extent of rupture in great earthquakes and improve the characterization of seismic hazards in subduction zones.

The surface coverage of regional reflection profiles probing the deep structure of the Cascadia subduction zone north of the Olympic peninsula is shown in Fig. 1. New images formed by processing the 1998 SHIPS[7] data significantly extend the study area and permit mapping variations in the reflection nature of the interplate interface, from the deep-sea deformation front to where the megathrust interface reaches the forearc mantle corner. Despite considerable variation in the reflection character of the subduction thrust on the seismic lines, there is a consistent downdip change from a thin (<2 km) reflection zone offshore to a broad reflection band (E-layer) some 5 to 7 km thick, inland of the west coast of Vancouver Island (Fig. 2).

In Fig. 3, we show two reflection transects across the northern Cascadia subduction zone formed by combining images from four reflection campaigns. The NE-trending transect (Fig. 3a; red lines in Fig. 1) extends from the deformation front to the east coast of Vancouver Island. The SE-trending transect (Fig. 3b; green lines in Fig. 1) extends from just offshore of Vancouver Island, where it crosses the SW–NE transect, to the eastern end of the Juan de Fuca Strait. Most of the reflection images in Fig. 3 are shown superimposed on a colour background representing tomographic P-wave velocities. The partially imaged interplate interface at the western half of the NE-trending transect (line 85-01 in Fig. 3a) is mostly characterized by a single reflection (as in Fig. 2a). The interplate interface appears to shallow landward of 40 km on the line 85-01 time section (Fig. 3a). This is a pull-up effect caused by a large lateral velocity change in the top 3–4 km of the crust. The subducting slab in this area is likely to have a smoother and more uniformly landward dipping geometry, similar to the one observed in Fig. 3b.

At the eastern end of line 85-01, the thrust reflection broadens into the 1.5 to 2 s (~5–7 km) wide E-reflection zone that extends through much of land line 84-01 and then abruptly ends. Reflections from the oceanic Moho are visible intermittently along line 85-01 and at the very western end of line 84-01. The Moho reflection is weak and has a similar shape to that of the megathrust event but is found at a recording time about 1.5 to 2 s later (5–7 km deeper). The E-reflection zone is imaged over the full length of the NW–SE transect (Fig. 3b). At the western end of line 85-05 the E-reflection zone is relatively thin (2–3 km). It gradually thickens landward reaching up to 8 km near the end of line 85-05, and is clearly visible

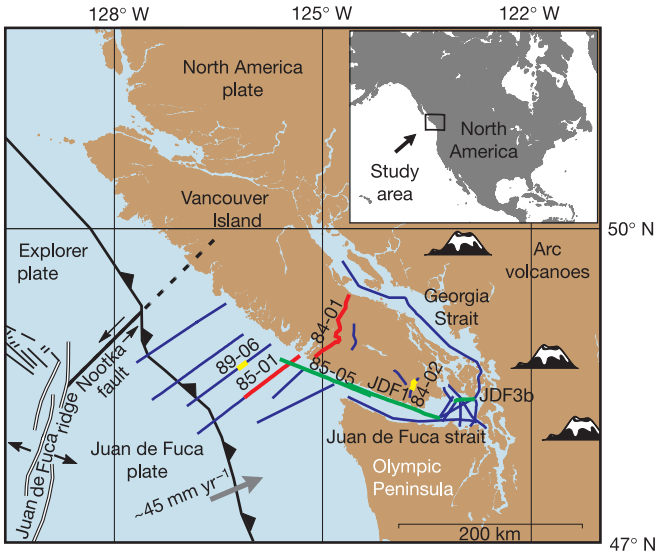

Figure 1 Simplified tectonic map of the northern Cascadia subduction zone. Purple, green and red lines are regional seismic reflection profiles. Four lines located on Vancouver Island were collected in 1984 as part of the Lithoprobe project. Nine lines found offshore of Vancouver Island were shot in 1985 for the Frontier Geoscience project of the Geological Survey of Canada, and in 1989 for the Geological Survey of Canada as part of the Ocean Drilling Program site survey. Profiles in the Strait of Georgia and Strait of Juan de Fuca were collected in 1998 during the SHIPS (Seismic Hazards Investigations in Puget Sound) experiment[7]. Short yellow lines show the surface location of the two details in Fig. 2. Red and green lines indicate the surface trace of the two reflection transects shown in Fig. 3. The inset shows the location of the tectonic map with respect to North America.

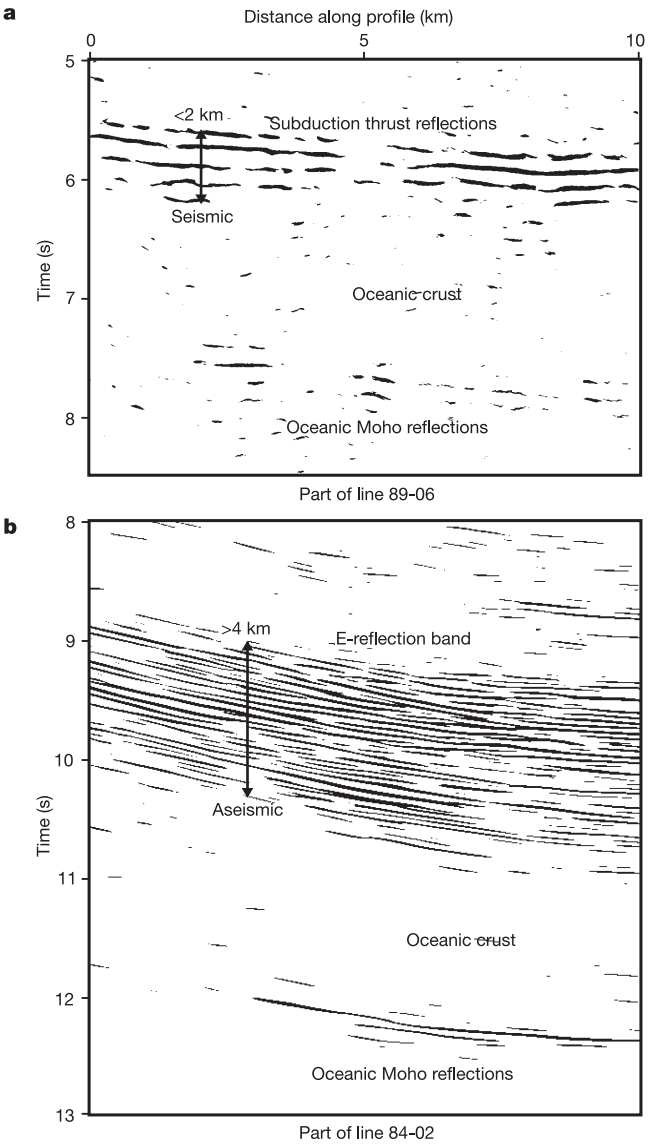

Figure 2 Two details showing the variation in the reflection character at the subduction thrust. **a**, Thin (<2 km) reflection response from the subduction thrust below line 89-06. The thrust is probably represented by a single reflection or a thinner reflection zone (<0.5 km) but the deconvolution was not able to remove the ringing and the stacking was not optimal, passing only the very low part of the signal spectrum. **b**, Thick (>4 km) band of reflections imaged on the most southern Vancouver Island line 84-02 overlies the subducted oceanic crust. In the initial Lithoprobe sections this thick, strong and landward dipping reflection band was named the 'E-layer' because it lies below a series of shallower reflections (A–D)[10]. To be compatible with the early interpretations we keep the name but in this work 'E' stands for 'electrically highly conductive'.

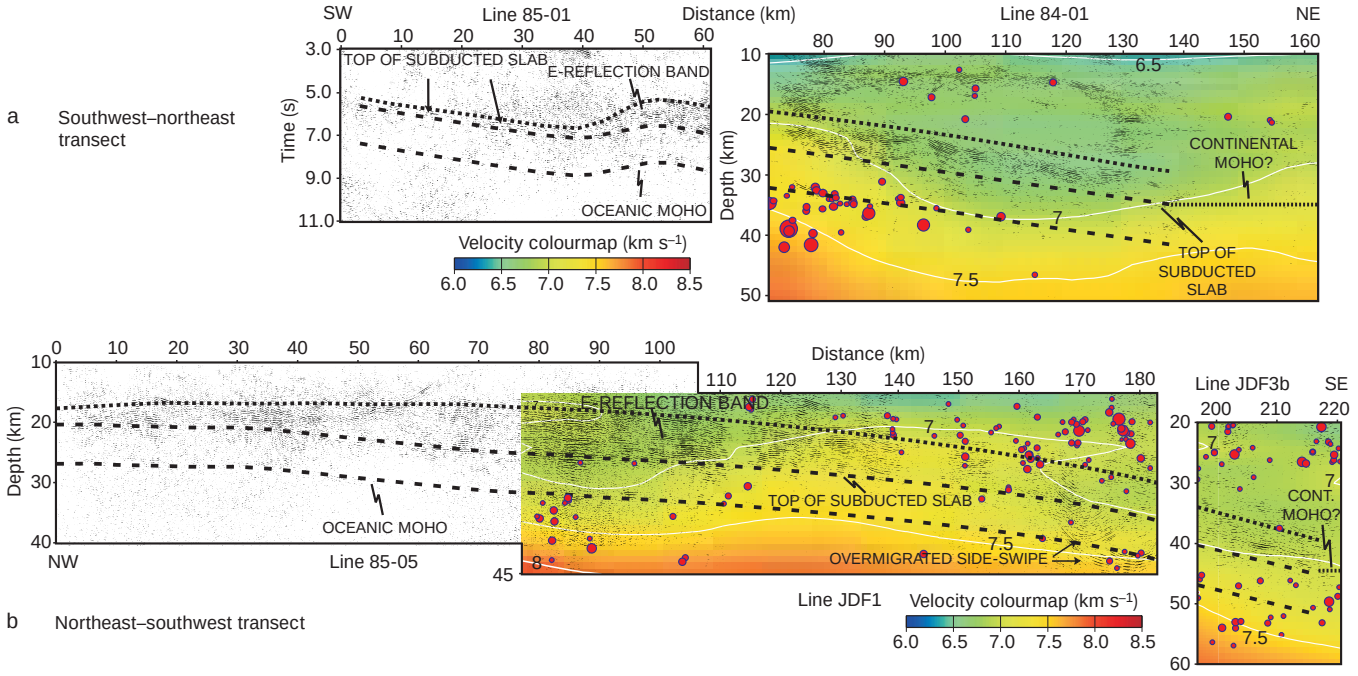

Figure 3 Two reflection transects across the northern Cascadia subduction zone. **a**, The 160-km-long NE-trending transect comprises profiles 85-01 and 84-01. **b**, The 220-km-long SE-trending transect comprises profiles 85-05, JDF1 and JDF3b. The presented images are time-migrated stacks. All except the 1985-01 image were converted to depth along vertical rays. Data from various campaigns were acquired using different equipment and were differently processed, resulting in non-uniform images. Only the depth or time range of interest is shown. P-wave tomographic velocities[24], extracted from a 3D velocity volume covering much of the study area, are shown as colour background for profiles 84-01, JDF1 and JDF3b. The tomographic velocities were computed by simultaneously inverting first P-wave arrivals from both the SHIPS 1998 wide-angle data set[7] and a selected earthquake data set[24]. Relocated seismicity from 50-km-wide swaths centred on the profiles is projected on the reflection images and is shown as circles whose size corresponds to earthquake magnitude (1.0–4.6). The ~1-s pull-up structure at about 40–50 km on line 85-01 is caused by a large lateral velocity change at the boundary between the Eocene fossil trench and the Pacific Rim terrain, located further landward. Sediments in the fossil trench are more than 3 km (~2.3 s) thicker than over the neighbouring Pacific Rim terrain, and show significantly lower average velocities (~3 km s^{-1})[28] than the rocks of the Pacific Rim terrain (5.25 km s^{-1})[29].

along lines JDF1 and JDF3b. The oceanic Moho is partially imaged along line 85-05 and at the western end of line JDF1.

The E-reflection band is regionally extensive (Fig. 4a) and where fully developed, it is 5 to 8 km thick. This band is present on all 1998 Juan de Fuca lines except for the easternmost S-trending line, on all 1984 Vancouver Island lines, on the 85-05 offshore line, and at the landward end of a number of other 1985 and 1989 offshore lines. The interpretations proposed for the nature of the E-reflection band can be divided into two classes, structural and nonstructural[8]. In the structural interpretations, the E-reflection zone is represented by interlayered mafic and/or sedimentary rocks[9,10], or intensely sheared sediments that trap fluids released from the subducting plate[11]. In the nonstructural interpretation, the E-reflection zone is caused by thin dipping lenses of high porosity, where the fluid is supplied by dehydration reactions within the subducted oceanic slab[12].

We believe that the E-reflections are related to both shearing and fluids, with the bulk of reflections caused by shearing. Temperature estimates on the megathrust[5] and fluid-filled porosity estimates within the E-reflection zone[12,13] lead us further to propose that ductile banding is the prevailing type of deformation in the E-layer shear zone. Laboratory and field studies of rocks from now-exposed deep faults and shear zones show that at depths of 10 to 15 km or more and temperatures above 250 to 350 °C, ductile processes begin to dominate and mylonites are formed[14]. The depth at which the E-reflection band is observed is everywhere greater than about 15 km (Fig. 3). The temperature at the base of the E-reflection band at its seaward limit is about 400 °C, increasing to about 500 °C at its landward limit.

Mylonite zones from exhumed ductile shear zones are often as wide as the E-reflection band[15] and are in most cases inferred to be very reflective even in the absence of water[14]. However, the E-reflection band must contain significant fluid-filled porosity to explain its high electrical conductivity[12,13], and inferred high Poisson's ratio[16]. The fluid paths are probably well interconnected because high tomographic P-wave velocities restrict this porosity to only a few per cent[12]. The E-reflection band may represent subducted and metamorphosed sediments. Alternatively, because the obtained tomographic velocities appear to be high for fluid-filled and sheared metasediments, perhaps the shearing cuts up into the overlying ductile forearc crust. The latter process should result in crustal material being transported to greater depths.

The E-reflections appear to end abruptly approximately where the subduction thrust encounters the forearc mantle wedge. For the SW–NE transect the E-reflections end at a depth of about 33 ± 3 km. Early two-dimensional (2D) seismic refraction data provide a depth of 37 ± 1 or 2 km for the continental Moho forming the lid of the forearc mantle wedge[17]. The original error estimate on the continental Moho depth should be increased to ±3 or 4 km, since the new tomography volume shows that the velocity structure is complex and highly three-dimensional. The continental Moho in the area could also be ~6 km shallower than previously interpreted, and therefore in better agreement with our results (Fig. 3a), because the strong wide-angle reflections in the early 2D refraction data recorded on Vancouver Island may well be from the subducting Moho and not from the continental Moho. Recent interpretations[18,19] show that wide-angle reflections from the continental Moho are very weak in the region of the forearc mantle wedge because mantle here is probably serpentinized and the velocity contrast at the continental Moho is very small. Free slip between the oceanic plate and the stable-sliding serpentinized rocks

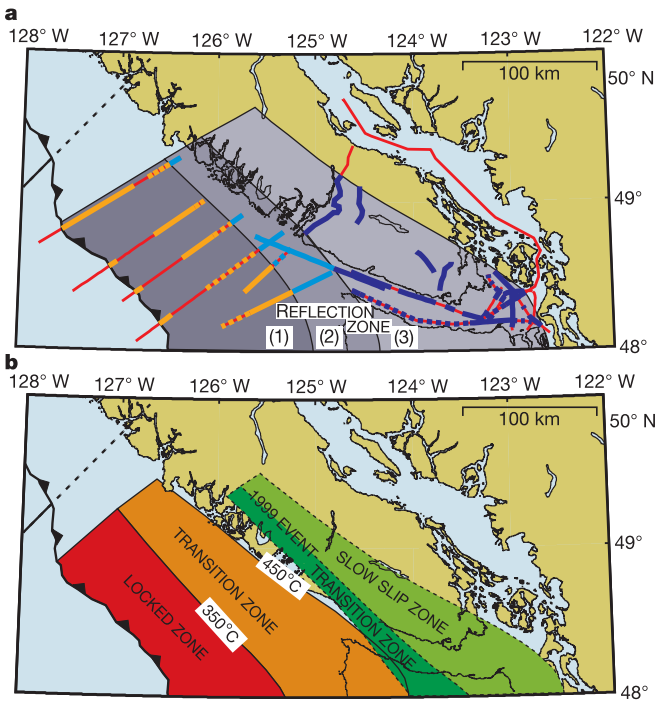

Figure 4 Locked seismogenic, transition, and stable slipping sections of the northern Cascadia subduction interface. Sections inferred from **a**, the extent and character of the subduction thrust reflections and **b**, thermal and dislocation studies[5], and dislocation modelling of the 1999 slow slip event[6]. **a**, Reflection zone 1 is characterized by thrust reflections less than 2 km thick. Zone 3 has a reflection band immediately above the oceanic plate that is more than 4 km thick. Within zone 2, this reflection band thickens from <2 to >4 km. Three-dimensional geometry of the subducted slab was taken into account when plotting the extent of the reflection zones. Thin red lines are reflection profiles. Overlying thick orange, blue, and purple lines indicate respectively where thin thrust reflections, transition to thick E-reflection band, and fully developed E-layer were successfully imaged. Dashed lines with identical colour-code and thickness show areas where imaging was intermittent. **b**, The location of the downdip thermal limit for seismogenic behaviour, inferred to be about 350 °C from laboratory and field studies, has been estimated from numerical modelling across the Vancouver Island margin[5]. The landward limit of the locked zone has been estimated by matching the predicted vertical and horizontal deformation from elastic dislocation models for a locked fault, to observations of repeated levelling surveys, global positioning system and other geodetic data[6,30].

of the overlying upper mantle has been proposed for greater depths[20]. The contact zone in this area of the thrust is probably quite thin, although there is some indication from the deep reflection profiles across the forearc of Chile that the broad reflection zone may continue below the forearc mantle wedge[21,22].

Our relocated seismicity, tomographic velocities, and reflection images (Fig. 3) indicate that the E-reflection zone lies just above the subducting oceanic slab. This identification is in agreement with some earlier interpretations[9,10] although several other studies[8,11,23] suggested that the E-reflection band is several kilometres above the subducting plate. Tomographic velocities from first-arrival data[24] (Fig. 3) only approximately outline the oceanic Moho, because of a 3-km cell size and a minimum structure assumption in the inversion. However, new 2D velocity models in Juan de Fuca Strait[25] were interpreted by inverting both refracted and reflected arrivals, including Moho reflections. These better constrain the oceanic Moho and infer that the top of oceanic crust is directly beneath the E-layer. The seismicity data suggest that a depth separation greater than about 2 to 3 km between the E-reflections and the oceanic plate cannot be accommodated, because relocated slab events occur within the top few kilometres below the E-layer (Fig. 3). The E-reflection zone itself appears to be mostly aseismic. Only a small number of earthquakes occur within this zone at the landward end of line JDF1, and these may be explained by a few events being poorly located. It is thus likely that the E-layer represents the current slow slip zone.

In Fig. 4, we compare the variations in reflection character along the subduction thrust with the extent of the locked, transition and stable sliding zones determined from thermal and deformation studies: (1) The locked seismogenic zone correlates with the generally thin megathrust reflection package (zone 1). (2) The modelled transition zone correlates with the zone of gradual thickening of the E-zone reflections (zone 2). (3) The fault area that moved in the well-defined 1999 and other slow slip events[6] correlates with the fully developed E-zone reflection package (zone 3). (4) The landward termination of the modelled 1999 slow slip area approximates the location of the abrupt termination of the E-zone reflections.

Our evidence suggests that the fully developed E-reflection zone demarcates the part of the subduction thrust where stable sliding and slow slip events dominate. Seaward thinning of the E-reflections delineates the transition zone towards the seismogenic part of the interplate interface that is characterized by narrow thrust reflections. The landward edge of the locked zone on the northern Cascadia subduction thrust inferred by reflection imaging appears to lie some 25–30 km closer to the land than estimated from thermal and dislocation modelling, implying a wider zone of coupling than currently proposed. If this wider zone is confirmed, a somewhat greater megathrust seismic hazard is suggested at inland cities. The transition zone based on reflection imaging is significantly narrower than the transition zone, as outlined by both thermal and dislocation modelling.

At the northern Cascadia subduction zone, deep reflection imaging has provided us with a method for detailed mapping of the expected rupture area of the subduction thrust, especially its landward limit, resulting in improved seismic hazard characterization. More accurate mapping of locked seismogenic zones requires calibration of the presented method at a subduction zone that has experienced megathrust earthquakes with the rupture extent defined by aftershocks and geodetic data. Deep seismic reflection images from Alaska[26], Chile[21] and SW Japan[27] show a similar broad reflection band above the subduction thrust in the region of stable sliding and thin thrust reflections further seaward, perhaps suggesting that reflection imaging may be a globally important predictive tool for determining the maximum expected rupture area in megathrust earthquakes. □

Received 3 January; accepted 18 June 2003; doi:10.1038/nature01840.

1. DeMets, C., Gordon, R. G., Argus, D. F. & Stein, S. Current plate motions. *Geophys. J. Int.* **101,** 425–478 (1990).
2. Heaton, T. H. & Hartzell, S. H. Earthquake hazards on the Cascadia subduction zone. *Science* **236,** 162–168 (1987).
3. Goldfinger, C., Nelson, C. H., Johnson, J. E. and the Shipboard Scientific Party. Holocene earthquake records from the Cascadia subduction zone and northern San Andreas fault based on precise dating of offshore turbidites. *Annu. Rev. Earth Planet. Sci.* **31,** 555–577 (2003).
4. Satake, K., Shimazaki, K., Tsuji, Y. & Ueda, K. Time and size of a giant earthquake in Cascadia inferred from Japanese tsunami records of January 1700. *Nature* **379,** 246–249 (1996).
5. Hyndman, R. D. & Wang, K. The rupture of Cascadia great earthquakes from current deformation and thermal regime. *J. Geophys. Res.* **100,** 22133–22154 (1995).
6. Dragert, H., Wang, K. & James, T. S. A silent slip event on the deeper Cascadia subduction interface. *Science* **292,** 1525–1528 (2001).
7. Fisher, M. A. *et al.* Seismic survey probes urban earthquake hazards in Pacific Northwest. *Eos Trans.* **80,** 16–17 (1999).
8. Calvert, A. J. Seismic reflection constraints on imbrication and underplating of the northern Cascadia convergent margin. *Can. J. Earth Sci.* **33,** 1284–1307 (1996).
9. Yorath, C. J. *et al.* Lithoprobe, southern Vancouver Island: seismic reflection sees through Wrangellia to the Juan de Fuca plate. *Geology* **13,** 759–762 (1985).
10. Clowes, R. M. *et al.* Lithoprobe - southern Vancouver Island: Cenozoic subduction complex imaged by deep seismic reflections. *Can. J. Earth Sci.* **24,** 31–51 (1987).
11. Calvert, A. J. & Clowes, R. M. Deep, high-amplitude reflections from a major shear zone above the subducting Juan de Fuca plate. *Geology* **18,** 1091–1094 (1990).
12. Hyndman, R. D. Deep seismic reflectors, electrically conductive zones, and trapped water in the crust over a subducting plate. *J. Geophys. Res.* **93,** 13391–13405 (1988).

13. Kurtz, R. D., DeLaurier, J. M. & Gupta, J. C. The electrical conductivity distribution beneath Vancouver Island: A region of active plate subduction. *J. Geophys. Res.* **95,** 10929–10946 (1990).
14. Jones, T. D. & Nur, A. The nature of seismic reflections from deep crustal fault zones. *J. Geophys. Res.* **89,** 3153–3171 (1984).
15. Higgins, M. W. Cataclastic rocks. *Prof. Pap. US Geol. Surv.* **687** (1971).
16. Cassidy, J. F. & Ellis, R. M. Shear wave constraints on a deep crustal reflective zone beneath Vancouver Island. *J. Geophys. Res.* **96,** 19843–19851 (1991).
17. Spence, G. D., Clowes, R. M. & Ellis, R. M. Seismic structure across the active subduction zone of western Canada. *J. Geophys. Res.* **90,** 6754–6772 (1985).
18. Bostock, M. G. *et al.* An inverted continental Moho and serpentinization of the forearc mantle. *Nature* **417,** 536–538 (2002).
19. Brocher, T. M. *et al.* Seismic evidence for widespread serpentinized forearc upper mantle along the Cascadia margin. *Geology* **31,** 267–270 (2003).
20. Peacock, S. M. & Hyndman, R. D. Hydrous minerals in the mantle wedge and the maximum depth of subduction thrust earthquakes. *Earth Planet. Sci. Lett.* **26,** 2517–2520 (1999).
21. Buske, S. *et al.* Broad depth range seismic imaging of the subducted Nazca slab, North Chile. *Tectonophysics* **350,** 273–282 (2002).
22. Oncken, O. *et al.* Seismic reflection image revealing offset of Andean subduction-zone earthquake locations into oceanic mantle. *Nature* **397,** 341–344 (1999).
23. Hyndman, R. D., Yorath, C. J., Clowes, R. M. & Davis, E. E. The northern Cascadia subduction zone at Vancouver Island: seismic structure and tectonic history. *Can. J. Earth Sci.* **27,** 313–329 (1990).
24. Ramachandran, K. *Velocity Structure of SW British Columbia and NW Washington from 3-D Non-linear Seismic Tomography.* PhD thesis, Univ. Victoria, 1–198 (2001).
25. Graindorge, D. *et al.* Crustal structure beneath Strait of Juan de Fuca and southern Vancouver Island from seismic and gravity analysis. *J. Geophys. Res.* (in the press).
26. Fisher, M. A., Brocher, T. M., Nokleberg, W. J., Plafker, G. & Smith, G. L. Seismic reflection images of the crust of the northern part of the Chugach Terrane, Alaska: Results of a survey for the Trans-Alaska Crustal Transect (TACT). *J. Geophys. Res.* **94,** 4424–4440 (1989).
27. Kodaira, S. *et al.* Structural factors controlling the rupture process of a megathrust earthquake at the Nankai trough seismogenic zone. *Geophys. J. Int.* **149,** 815–835 (2002).
28. Langston, S. *The Seismic Structure of Tofino Basin and Underlying Accreted Terrains*. MSc thesis, Univ. Victoria (1995).
29. Clowes, R. M. *Crustal Structure of the Northern Juan de Fuca Plate and Cascadia Subduction Zone—New Results, Old Data* 55–58 (US Geol. Surv. Open-File Report 02-328 and Geol. Surv. Can, Open File 4350, 2002).
30. Wang, K. *et al.* A revised dislocation model of the interseismic deformation of the Cascadia subduction zone. *J. Geophys. Res.* **108**(B1), 101029/2001JB001703 (2003).

Acknowledgements We thank M. Fisher, T. Brocher, and many other participants for their part in organizing and carrying out the 1998 SHIPS experiment. The land seismic reflection data were collected as part of the Lithoprobe project. M.R.N. is grateful to S. Carbotte for allowing him to complete this work while he was a Post Doctoral Research Scientist at the Lamont-Doherty Earth Observatory of Columbia University. We thank T. Brocher for a series of critical reviews, A. Calvert and S. Mazzotti for discussions, and the Lamont-Doherty Earth Observatory of Columbia University for financially supporting the publication of this paper.

Competing interests statement The authors declare that they have no competing financial interests.

Correspondence and requests for materials should be addressed to M.R.N. (mladen@ldeo.columbia.edu.).

Catastrophic extinctions follow deforestation in Singapore

Barry W. Brook*†, Navjot S. Sodhi‡ & Peter K. L. Ng‡

** Center for Ecological Research, Kyoto University, Otsu 520-2113, Japan*
† Key Centre for Tropical Wildlife Management, Northern Territory University, Darwin 0909, Northern Territory, Australia
‡ Department of Biological Sciences, National University of Singapore, 14 Science Drive 4, Singapore, 117543, Republic of Singapore

The looming mass extinction of biodiversity in the humid tropics is a major concern for the future[1], yet most reports of extinctions in these regions are anecdotal or conjectural, with a scarcity of robust, broad-based empirical data[2–4]. Here we report on local extinctions among a wide range of terrestrial and freshwater taxa from Singapore (540 km^2) in relation to habitat loss exceeding 95% over 183 years[5,6]. Substantial rates of documented and inferred extinctions were found, especially for forest specialists, with the greatest proportion of extinct taxa (34–87%) in butterflies, fish, birds and mammals. Observed extinctions were generally fewer, but inferred losses often higher, in vascular plants, phasmids, decapods, amphibians and reptiles (5–80%). Forest reserves comprising only 0.25% of Singapore's area now harbour over 50% of the residual native biodiversity. Extrapolations of the observed and inferred local extinction data, using a calibrated species–area model[7–9], imply that the current unprecedented rate of habitat destruction in Southeast Asia[10] will result in the loss of 13–42% of regional populations over the next century, at least half of which will represent global species extinctions.

Tropical forests represent the Earth's major reservoir of terrestrial biodiversity[4,11], yet these biomes are now gravely imperilled by anthropogenic change, including deforestation and habitat degradation[12,13], overexploitation of plant and animal populations[14], and the introduction of invasive species[1]. If we are to avert or at least mitigate catastrophic loss of species in these areas, it is vital to

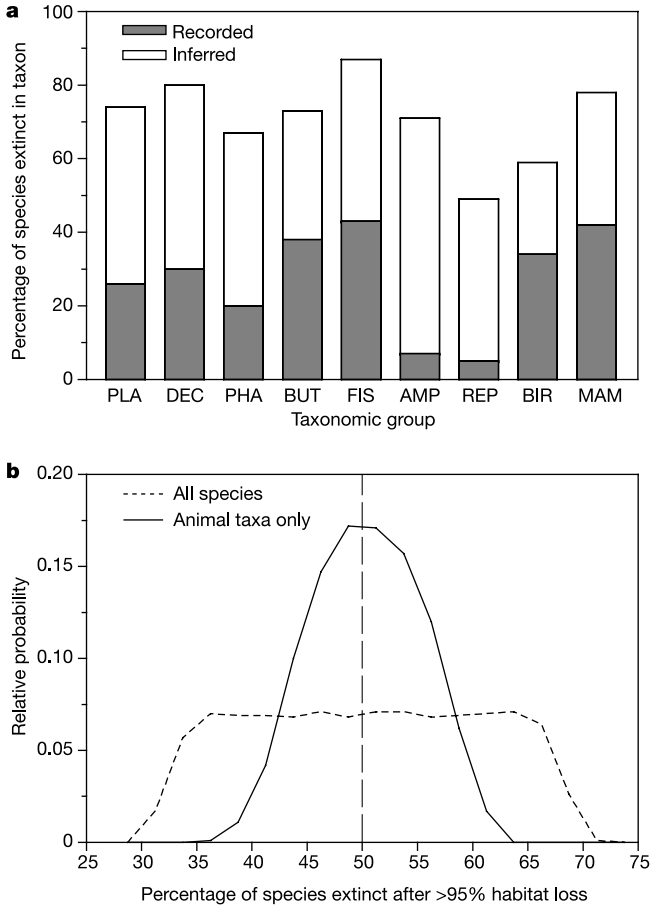

Figure 1 Observed and projected biodiversity loss in Singapore, 1819–2002. **a**, Observed (recorded) and inferred extinction rates for vascular plants (PLA; number of modern, historically recorded and inferred species is 1,683, 2,277 and 6,549, respectively), freshwater decapod crustaceans (DEC; 16, 23, 82), phasmids (PHA; 33, 41, 100), butterflies (BUT; 236, 381, 863), freshwater fish (FIS; 35, 61, 269), amphibians (AMP; 25, 27, 87), reptiles (REP; 117, 123, 228), birds (BIR; 144, 218, 347) and mammals (MAM; 26, 45, 117). **b**, Combining the data from **a** provides a probability distribution of potential total species extinctions for all taxa (dashed line) and animal taxa only (continuous line), given a habitat loss exceeding 95% over a 183-year period. This was derived via computer re-sampling of the extinction data by assuming that the true extinction rate was equally and independently likely to lie anywhere between the observed and inferred proportions for each taxa. The vertical line indicates the mean of the animal taxa distribution.